

UNSTEADY SIMULATION OF THE FLOW DURING THE DEPLOYMENT OF HIGH-LIFT SYSTEMS

Nicolas Renard¹, Jochen Wild²

¹ Ecole Polytechnique ParisTech
F-91128 Palaiseau, France
nicolas.renard.2008@polytechnique.org

² DLR Institute of Aerodynamics and Flow Technology
Lilienthalplatz 7, 38108 Braunschweig, Germany
Jochen.wild@dlr.de

Keywords: high-lift systems aerodynamics, unsteady CFD, Chimera method, aerospace engineering

Abstract. *This study focuses on the numerical simulation of the unsteady two-dimensional flow during the deployment and retraction of the slats and flaps of a transport aircraft wing section, using the compressible unsteady RANS solver DLR Tau with the Chimera technique.*

The unsteady lift coefficient of the flap moving alone can be predicted by quasi-steady corrections. The motion of the slat has a much more complicated impact on the flow. Generally speaking, the time-delays are high. The unsteady simulations reveal a sudden growth of the flow separation on the flap after the end of the movement of the devices.

The Chimera method enables a great flexibility, but it introduces significant numerical disturbances for both steady and unsteady solutions. This study shows that they are mainly caused by interpolations performed from a fine mesh to a mesh having a lower resolution.

A Fourier analysis reveals a low-frequency oscillation which may be an eigenmode of the flap. It also reveals how the vortex shedding predicted at the trailing edge of the flap develops when the slat and the flap have stopped moving.

The reliability of these results still has to be assessed thanks to other numerical simulations, as wind-tunnel or in-flight tests seem unfeasible.

1 INTRODUCTION

High-lift systems enable transport aircraft, which are optimized for cruise flight at high airspeeds, to take off and land safely at a much lower airspeed. The maximum lift coefficient of the aircraft must be raised by increasing the projected wing area and camber, and thereby increasing the intrinsic maximum lift coefficient.

The design and test process of transport aircraft leads to a good knowledge of the steady behavior of high-lift systems. However, little is known about the unsteady flow during the deployment and the retraction. Although the deployment speed is relatively low, unsteady effects are assumed to be significant. Due to the large deployment of the high-lift system elements, the steady flows in the retracted position and in the fully extended position are completely different from each other.

Knowing these unsteady features could improve the accuracy of flight dynamics models. These models are crucial for the development of fly-by-wire systems and autopilots, as well as for realistic flight simulation. It could also be crucial to know those features if a faster deployment mechanism were to be designed, which would trigger stronger unsteady effects. Besides, describing the unsteady flow can help to reduce low frequencies that may arise during the motion of the high-lift system and make the travel uncomfortable.

Unfortunately, either in-flight measurements or wind-tunnel experiments seem technically to require extremely high efforts. One option left to assess these unsteady effects is numerical simulation, which is the goal of this work. The present study analyses the unsteady flow features appearing at a 3-element high-lift airfoil during deflection and retraction of the high-lift system. The unsteady flow during the deployment and retraction of the high-lift systems of transport aircraft has been numerically simulated in order to assess differences to the steady state solution at extreme and intermediate high-lift device positions.

Beside applying a state-of-the-art unsteady RANS solver the Chimera, or overset grid method, is seen as a key technology for the simulation of the flow around several bodies moving relatively to each other. The grids around the components of the multi-element airfoil are kept throughout the simulation process. Therefore there is no influence of changing grids on the quality of the flow solution.

2 DEFINITION OF THE CASE IN STUDY

2.1 High-lift devices and aircraft type considered in this study

There are many kinds of high-lift devices, as described in [1]. This study considers a wing section of a generic high-lift wing, the DLR-F15 [2], which is representative for today's transport aircraft high-lift system layout. It is equipped with a slat and a single-slotted Fowler flap.

Figure 1 shows several settings of the system. The slat moves in a rotational motion forwards and downwards. A slot appears between the leading edge of the main wing and the slat when deployed. Fowler flaps move backwards, so as to increase the wing area and to create a slot between the main wing and the flap, and rotate downwards, so as to load them aerodynamically. For take-off, it is crucial that the lift-drag ratio is as high as possible (see [1]), so the flaps must first be moved backwards so as to get as high a Fowler motion as possible. On the other hand, the drag generated by the flaps can be useful for the approach, so the end of the deployment sequence mainly increases the deployment angle further.

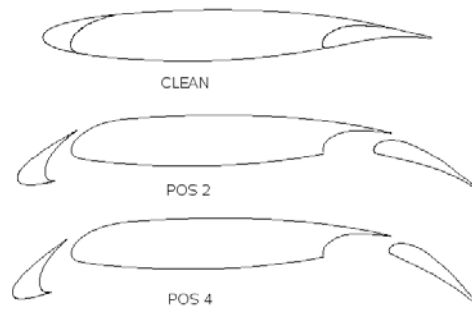


Figure 1: DLR F15 3-element airfoil in designated positions clean, take-off (pos 2) and landing (pos 4)

2.2 Two-dimensional approximation

Slats extend along almost the full wing span, and flaps about 60-80% of the span. The DLR-F15 wing section is taken at a mid-span location of the reference wing, so the computation of a 2D flow should give a good idea of some of the effects triggered by flaps and slats deployment on the flow about the complete 3D wing, although purely 3D effects are missing.

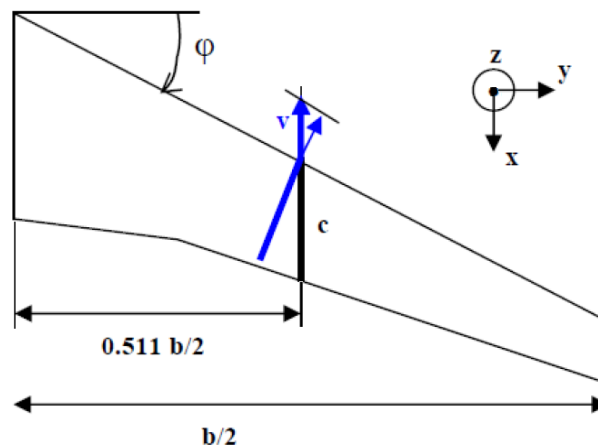


Figure 2: Two-dimensional case definition

As shown on Figure 2 the wing section taken in line of flight is transformed into a coordinate system perpendicular to the leading edge to best describe the flow characteristics of the 3D wing. This leads to the simpler case of a wing of infinite span and constant chord length, the sweep angle of which ($\varphi = 30^\circ$ at the leading edge) is taken into account by normalizing the airfoil accordingly. The flow is decomposed into a component parallel to the leading edge, which is assumed not to be disturbed by the wing, and a component orthogonal to the leading edge, which is the one considered in the 2D computation.

The leading edge normalization additionally results in the following scaling rules for the flow conditions and the results of the 2D computations:

$$\begin{aligned}
 M_{2D} &= M_{3D} \cdot \cos(\varphi) \\
 Re_{2D} &= Re_{3D} \cdot \cos^2(\varphi) \\
 \tan(\alpha_{2D}) &= \tan(\alpha_{3D})/\cos(\varphi) \\
 C_{L,3D} &= C_{L,2D} \cdot \cos^2(\varphi)
 \end{aligned} \tag{1}$$

For all the following 2D computations, the Mach number was set to $M_{2D} = 0.15$ and the Reynolds number to $Re_{2D} = 7.10^6$, while the 2D chord length was set to $c_{2D} = 2$ m. The computations were performed at a constant angle of attack, which was arbitrarily set to $\alpha_{2D} = 10^\circ$, a value that is close to usual local angles of attack in low-speed flight, and these values are representative for the approach and landing flight parameters. The physical time scale itself is not affected by the transformation from 2D to 3D.

For this first step, the case considered is a deployment of the high-lift system during a straight and level flight with constant airspeed and angle of attack, which is not a real flight maneuver. Coupling with a flight dynamics simulation would be necessary to be more realistic.

2.3 Slat and flap kinematics

High-lift system settings are usually defined for a number of discrete settings, characterized by the deflection angle of the device. Similar to Airbus aircraft, for the DLR-F15 five named settings are specified that are listed in Table 1.

POSITION	SLAT deployment angle ($^\circ$)	FLAP deployment angle ($^\circ$)
0	0	0
1	17	0
1+F	17	14
2	22	23
3	22	35
4	28	35

Table 1: Leading and trailing edge devices settings

The positioning of the devices is furthermore depending on the underlying kinematics. The slat has a circular motion simply defined by its center of rotation (see Figure 3). On the contrary, the flap motion is more complicated. Indeed, the first part of the motion must mostly be Fowler motion, whereas the second part must rather change the deployment angle. To describe it, this study considers the link-track mechanism (see Figure 4), which is used for the Airbus A330 and A340.

Once the mechanism has been defined, it is possible to compute the path of the flap. To determine the deployment speed, the angular velocity of the flap actuator is considered constant. Unfortunately, the actuator is not working directly on the link (i.e. on angle φ_5 on Figure 4). The mechanism is linked to a rotating actuator in front of the track, with additional links and pivots described thanks to the software Teflames (Trailing Edge Flap Mechanism Synthesis, see [3]): see Figure 5. Finally, the resulting deployment time function is interpolated by three time-dependent high-order Lagrange polynomials suited for the 2D rigid body motion description module of the flow solver.

Deployment speeds were evaluated thanks to the parameters used for flight simulation at DLR and from a few videos of deployment sequences which can be found in the internet, such as [4]. For the slat, a constant angular velocity of $1.5^\circ/s$ is applied. For the flap, the mean angular velocity is $2.3^\circ/s$. Slats and flaps, in the model defined for this study, start simultaneously but may not necessarily reach their new position at the same time.

Table 2 presents the four unsteady cases, which have been simulated. They all represent motions between the settings for take-off and landing. A complete retraction of the system hasn't been possible due to limitations of the Chimera method. For instance, Case 24 refers to the deployment from take-off to landing position. The flap extends within the time $t = 0s$ to

$t = 2.6s$, then stops moving, while the slat extends from $t = 0s$ to $t = 4s$. Case 24 REV is the retraction case corresponding to Case 24, with a reversed motion, such that the retraction goes through the same settings as the deployment.

Case 24	time (s)	0.0	2.6	4.0
	Slat. angle (°)	22	>	28
	Flap. angle (°)	23	35	35
Case 24 REV	time (s)	0.0	1.4	4.0
	Slat. angle (°)	28	>	22
	Flap. angle (°)	35	35	23
Case 23	time (s)	0.0	2.6	
	Slat. angle (°)	22	22	
	Flap. angle (°)	23	35	
Case 34	time (s)	5.0	9.0	
	Slat. angle (°)	22	28	
	Flap. angle (°)	35	35	

Table 2: Definition of the unsteady cases

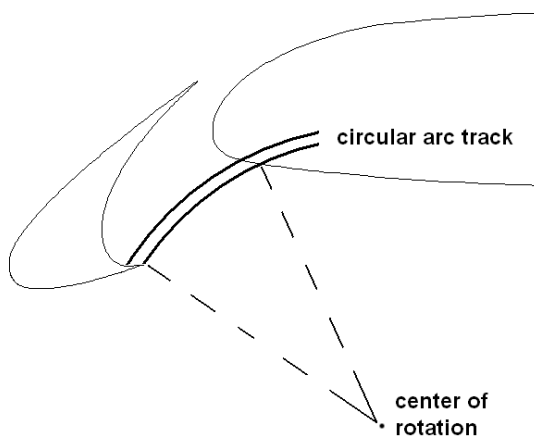


Figure 3: Slat kinematics

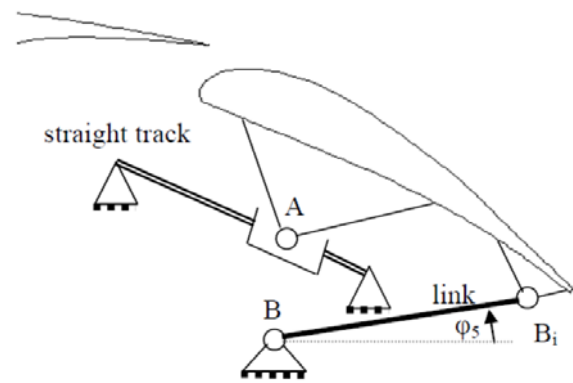


Figure 4: Link-track mechanism

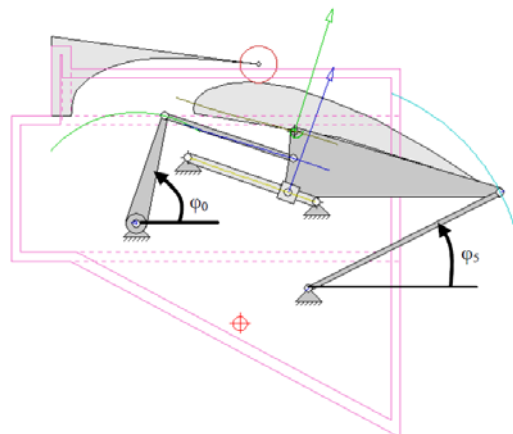


Figure 5: Flap mechanism in the Teflames software

3 PHYSICAL AND NUMERICAL MODELS

Although the upstream Mach number is relatively small, high lift systems can lead to high local Mach number values [5]. As a consequence, a compressible flow solver is required. Moreover, the combination of the three airfoil elements leads to complex viscous phenomena which require the resolution of the full Navier-Stokes equations.

Given the relatively high Reynolds number and the fact that slats do not allow a perfectly smooth upper surface, the whole flow is assumed to be turbulent. The Reynolds-Averaged Navier-Stokes equations with the Spalart-Allmaras turbulence model (in its original 1992 version) are solved by the DLR TAU code [6].

This flow solver uses a finite volume formulation of the equations, with a cell vertex grid metric. Control volumes are defined around each vertex, the value at the vertex being the averaged value on the control volume. The gradients are evaluated by a Green Gauss method. A central difference scheme is used to compute the inviscid fluxes with matrix dissipation.

Hybrid meshes have been used. The mesh for the main wing was generated using the Centaur commercial software [7], with a quasi-structured inner mesh layer to resolve the boundary layer and an unstructured outer mesh extending to the farfield boundary, which is a circle with a radius of 50 chord lengths. For the slat and the flap, structured meshes were made using Mega Cads [8], a grid generator developed at DLR. Each mesh provides a fine resolution in the vicinity of the wake of the airfoil element it surrounds. The overall number of points is 235000.

In order to compute the unsteady flow during the deployment of the high-lift system, the mesh must be adapted at each time step to the new geometry. Thanks to the Chimera method, it is possible to use the same three meshes (one for each element), whatever the positions of the flap and slat are.

To get a solution common to the three meshes, the chimera method consists of exchanging the values and the normal derivatives of the considered flow quantities at the frontier of the meshes at each iteration of the relaxation solver. Actually, in the TAU implementation of the Chimera method, the values of the two last rows of vertices, which are called "fringe points", are exchanged – see Figure 6. However, the two meshes do not match, so the exchange consists of an interpolation instead of a simple copy. At the beginning of every iteration, the fringe points of each mesh must be interpolated from values on the other mesh that are computed (and not interpolated) during the iteration. Hence there must be a sufficient overlapping between the two meshes, at least 2 rows of mesh cells on each side of the interfacing boundary. Since the same equations are solved on each mesh, it is not a problem if the overlapping is wider than necessary. The interpolation is made so as to conserve as well as possible quantities such as mass, momentum and energy. However, the Chimera method is not formally conservative.

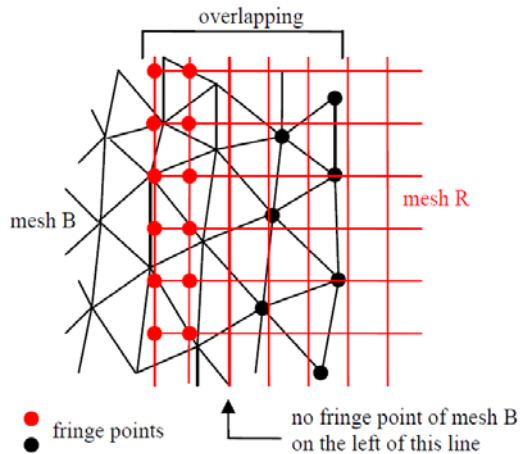


Figure 6: Chimera method

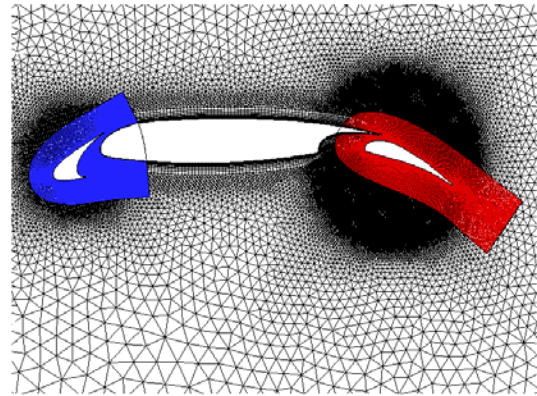


Figure 7: Chimera mesh

The definition of the overlapping, also called definition of the holes cutting, leaves much freedom to the user. In this study, the holes were defined as the airfoil elements themselves plus a given thickness, which is as small as possible so that it is possible to retract almost completely the high-lift system. Figure 7 shows the blanking of the meshes which was used for most of this work.

The relaxation solver uses an explicit 3-stage Runge-Kutta method in a fictitious pseudo-time, with local time stepping. Further convergence acceleration is achieved by means of residual smoothing and multigrid technique.

For unsteady time-accurate simulations, the physical time integration is made by an implicit second-order accurate scheme, the 2nd order Backward Difference Formula.

4 QUALITY MONITORING OF THE SOLUTIONS

4.1 Convergence monitoring

The degree of convergence of the solution has to be monitored to determine how many iterations of the relaxation solver are needed. One first way of achieving this consists of monitoring the density residual, which is the integral of the square of the difference of density between the actual value and the value at the previous iteration. However, even if the density residual has become much smaller, it is possible that the lift coefficient has not yet converged.

This study focuses on the first parameter of interest for high-lift systems, i.e. the lift coefficient. An accuracy of 0.001 is needed for this coefficient, because the unsteady effects caused by the deployment of the system seem to be of this order of magnitude. Of course, this is not an absolute accuracy, because the model cannot provide such reliable predictions. However, this relative accuracy is needed for comparisons with other simulations and with steady solutions computed with the same model. As a consequence, the convergence monitoring parameter was the lift coefficient, a good enough convergence of which the relaxation solver waits for.

4.2 “Steady” solutions computation

The comparison of the simulated unsteady flow with steady solutions is crucial. However, computing reliable steady solutions was a major problem. For instance, for the steady flow around the system in position 4, the steady state solver predicts, after 300000 iterations, a lift

coefficient close to 3.208, whereas the unsteady solution, once the system does not move any more, converges to a lift coefficient close to 3.204.

Since the steady solutions for this study were only computed for comparison purposes with the unsteady simulations, it was chosen to define in this work a “steady” solution as a time-averaged solution computed with the unsteady solver, set with the same physical time step as the unsteady simulations, with a frozen configuration of the system, waiting for the lift coefficient to converge in physical time.

4.3 Holes definition

The definition of the holes for the Chimera method determines the areas where values are interpolated from one mesh to the other. It is much more accurate that both meshes have similar resolutions where they overlap. Indeed, the value interpolated for a fringe point of a mesh A is taken from the cell of the other mesh B in which the fringe point is located. This means that if the control volume around the fringe point contains many (smaller) cells of the mesh B, because mesh B is finer than mesh A, then the value given to the fringe point is the value of the cell of the mesh B where the point is located, instead of the average of the value over the whole control volume of mesh A. This leads to inconsistencies in the areas of wakes: for instance, it can be seen on Figure 8 that in this case, the steady solution does not transmit properly the wake of the slat onto the mesh of the main wing.

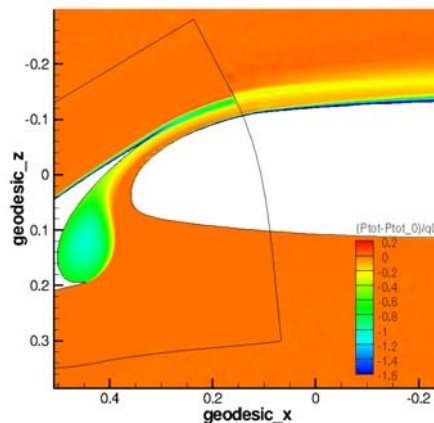


Figure 8: Steady solution for the setting at $t = 1.019$ s of Case 24. Total pressure.

The impact of the holes definition on the steady solutions is dangerously high. For the setting of time $t = 1.019$ s of Case 24, with the holes definition used for most of this study, the computed lift coefficient is 3.168, whereas it is 3.151 with another definition for which the cutting is made twice farther from the wall of each airfoil element. This gap is higher than the unsteady effects sought in this study.

4.4 Chimera unsteady issue

The Chimera method causes another major issue during unsteady simulations. Indeed, when the flap and the slat are being deployed, points of each mesh change status. Some points which were hidden by another element (*i.e.* blanked points) become fringe points, some fringe points become computed points, and the opposite evolutions may also happen. Figure 9 shows the resulting lift time-signal in Case 24 (see Table 2): each abrupt change of the lift coefficient corresponds to the evolution from a fringe point to a computed point in the area of the mesh of the flap in the region of the wake behind the trailing edge of the wing. The change of method how to obtain the values for such a point, namely switching from interpolation from a

much finer grid to computation based on the cell volume itself generates a sudden change of the flow state variables. The perturbation is conveyed by a pressure wave with relatively high an amplitude.

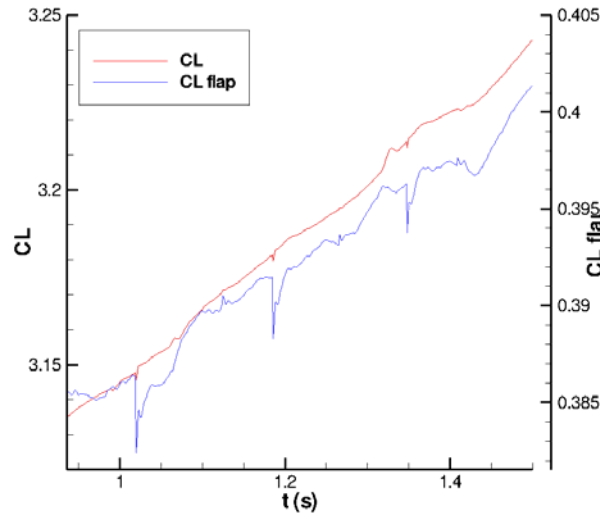


Figure 9: Lift coefficient, unsteady simulation of case 24

Almost the same perturbation happens when the system is being retracted instead of deployed. Figure 10 shows an approximation of the first time derivative of pressure, at the end of Case 24, when the slat is being deployed. Figure 11 shows exactly the same quantity, with the same setting of the system but with an opposite motion (Case 24 REV in Table 2): the slat is being retracted. The pressure perturbation looks strikingly similar in both cases.

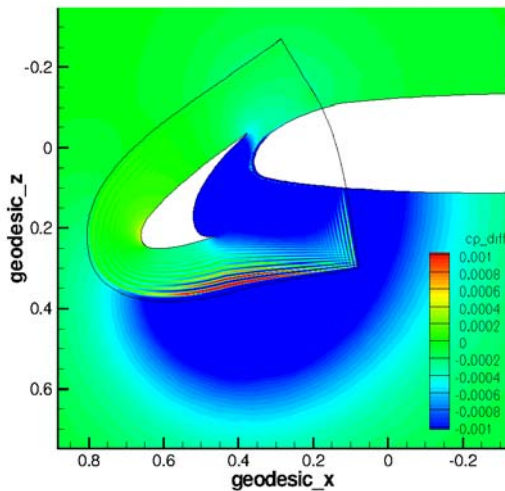


Figure 10: $C_p(t = 3.659 \text{ s}) - C_p(t = 3.658 \text{ s})$
Case 24 (deployment)

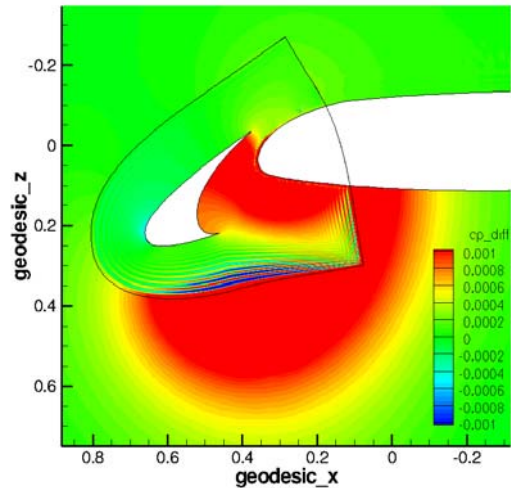


Figure 11: $C_p(t = 0.342 \text{ s}) - C_p(t = 0.341 \text{ s})$
Case 24 reversed (retraction)

Moreover, the lift perturbation has the same magnitude as the gap between the steady solutions computed for the setting of the considered time step and for the setting of the previous time step. This indicates that the Chimera unsteady issue is similar to the problem of the holes definition: adding one new point to the mesh in a critical area like the vicinity of a wake has a strong impact on the approximate solution computed.

Unfortunately, it seems difficult to avoid this issue, as it is impossible not to interpolate in the wakes of the airfoil elements. For this work, these numerical perturbations, although present, have been ignored, trying to recover the “physical” signal.

5 UNSTEADY FLOW RESULTS

5.1 Case 23: time delays

Figure 12 and Figure 13 show the global lift coefficients during Case 23 (see Table 2). The flap is deployed between $t = 0$ s and $t = 2.6$ s, whereas the slat does not move. The Chimera problem is easy to see and affects especially the lift coefficient of the flap.

Whereas the lift of the flap is very close to its steady value, the lift of the other elements seems to have some delay, especially for the slat. The analysis of time delays is done with respect to the characteristic times of the approximate one-dimension system describing the airfoil. With a chord length $c = 2$ m, a free-stream velocity $U_\infty = 49.7$ m/s and the free-stream speed of sound $a_\infty = 331$ m/s, three characteristic times can be derived: the advection time

$$\tau_a = \frac{c}{u_\infty} = 4.0 \cdot 10^{-2} s \quad \text{and the times for pressure waves propagating downstream}$$

$$\tau_{pd} = \frac{c}{a_\infty + u_\infty} = 5.2 \cdot 10^{-3} s \quad \text{and upstream} \quad \tau_{pu} = \frac{c}{a_\infty - u_\infty} = 7.1 \cdot 10^{-3} s .$$

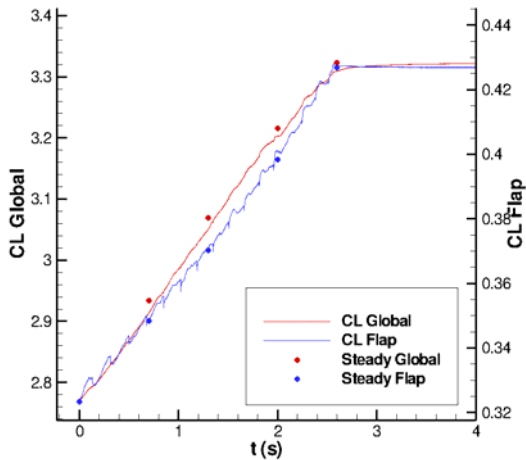


Figure 12: Case 23, Global and flap CL compared with steady solutions

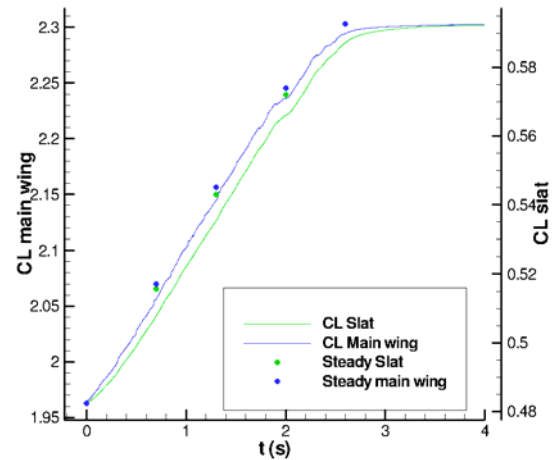


Figure 13: Case 23, Slat and main wing CL compared with steady solutions

The delay of the global C_L is equal to $1.9\tau_a$, and the delay of the slat is equal to $4.1\tau_a$. Pressure waves are much quicker than advection, but are not sufficient for the flow adaptation, which seems to be determined by the characteristic advection time of the airfoil τ_a .

The characteristic times can also be computed using as the characteristic length the distance between the farfield and the airfoil, i.e. 50 chord lengths (100m). The advection time is then 2.01s, the time for upstream pressure waves is 0.36s, and the time for downstream pressure waves is 0.26s. None of the information about the flap motion can reach the far-field in a shorter time than the measured time delay. Consequently, one may assume that the farfield boundary is far enough to have no impact on the time delays of the flow near the airfoil.

However, the time delay before the coefficients reach their steady value once the motion is over is much longer than the characteristic advection time defined for the airfoil. Only the ini-

tial response of the flap to the abrupt stop of its motion consists of a quick convergence to a value closer to the steady behavior, with a characteristic time close to 25ms. This time is roughly $2.3 \tau_{Fa}$, with the advection time for the flap defined as $\tau_{Fa} = \frac{c_F}{u_\infty} = 1.1 \cdot 10^{-2} s$, where $c_F = 0.561m$ is the chord of the flap.

These results suggest that the final convergence towards the steady values may depend on the farfield boundary distance, but this has not yet been investigated.

5.2 Case 23: quasi-steady corrections

In Case 23, for which only the flap is moving, the computed lift coefficient of the flap is very close to its steady value. This suggests that the time delay caused by the flow adaptation to the new geometry may have almost no impact on the flap. Then the unsteady effect affecting the flap would only result from the new no-slip boundary condition caused by the motion.

This effect is expected to introduce a small perturbation to the steady solution, resulting in a correction of the lift coefficient of the flap which is evaluated here. The main hypotheses are that the motion is very slow when compared to the free-stream velocity and that the time delays of the flow can be neglected. That is why these unsteady corrections will be called “quasi-steady”. No interaction between the three elements is taken into account.

The instantaneous motion of the flap results from a translation of its reference point and a rotation about the axis going through this point. The reference point is chosen as the quarter-chord point (see Figure 14), because it is located near the pressure center of the airfoil. It is then possible to compute a change of the angle of attack of the flap $\Delta\alpha$, the new norm U_{tot} of its relative airspeed and an angular velocity ω .

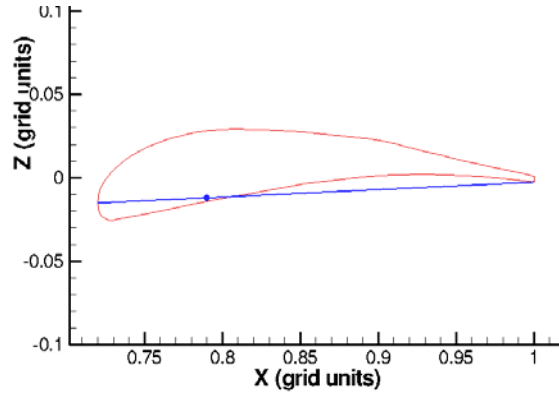


Figure 14: Flap chord and quarter-chord point

The local Mach number around the flap remains reasonably low and the Prandtl-Glauert factor (1.011) is close to 1. Since the purpose is only to evaluate the order of magnitude of the effect, the correction for the flap is simply computed as if the flow is incompressible. Thin airfoil theory is then applied, although the flap is relatively thick (more than 14% of the local chord).

The perturbation caused by the translation is evaluated in a 1st order approximation as the following, where c_{REF} is the reference chord of the whole airfoil, c the chord of the flap and U_∞ the free-stream velocity:

$$\Delta_{transl.} C_L = \frac{U_{tot}^2}{U_\infty^2} \cdot \left(C_L + \frac{c}{c_{REF}} \cdot 2\pi \cdot \Delta\alpha \right) - C_L \quad (2)$$

The effect of the rotation of the flap about its reference point is modeled by a distribution of vorticity imposed on the chord of the flap (the vorticity shed from the trailing edge has not been taken into account here), so that the no-penetration boundary condition still holds on the chord. However, the choice of the solution is usually based on the Kutta condition for steady flows. The angular velocity of the flap in this study does not exceed $6^\circ/\text{s}$. Reference [9] suggests that since the corresponding Strouhal number $St = \frac{\omega \cdot c}{U_\infty} = 1.2 \cdot 10^{-3}$ is much smaller than

1, as long as there is no massive flow separation on the flap, the Kutta condition should still hold, leading to the following perturbation of the lift coefficient of the flap:

$$\Delta_{rot.} C_L = \frac{\omega \cdot c^2 \cdot \pi}{U_\infty \cdot c_{REF}} \quad (3)$$

Finally, both effects are added in a kind of linearization of the quasi-steady solution near the steady solution:

$$C_{L, QS} = C_L + \Delta_{transl.} C_L + \Delta_{rot.} C_L \quad (4)$$

The results show that the effect of the rotation is almost one order of magnitude greater than the effect due to the translation. Figures 15 and 16 present examples of the results in Case 23. Dots show steady solutions, triangles quasi-steady corrected solutions, and the curves present the unsteady computation. The correction is surprisingly close to the actual unsteady value.

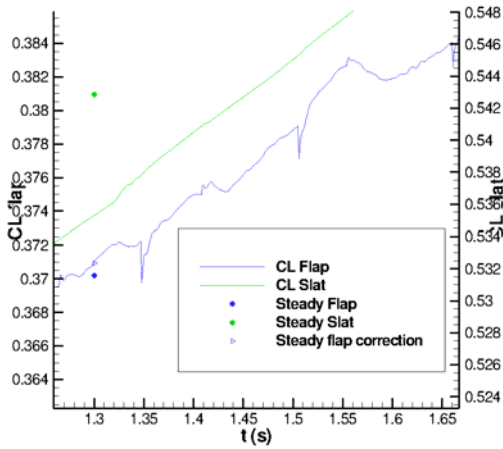


Figure 15: Case 23, $t = 1.3$ s

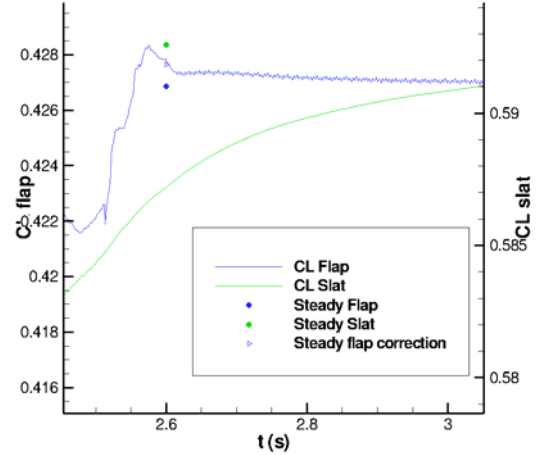


Figure 16: Case 23, $t = 2.6$ s

5.3 Cases 24 and 24 reversed

Figure 17 and Figure 18 present the lift coefficients for the cases 24 and 24 REV. Time is reversed for Case 24 REV, so that a given setting of the system is linked to a given position on the x axis. Both the flap and the slat are moving. The motion of the flap ends at $t = 2.6$ s and the motion of the slat ends at $t = 4$ s.

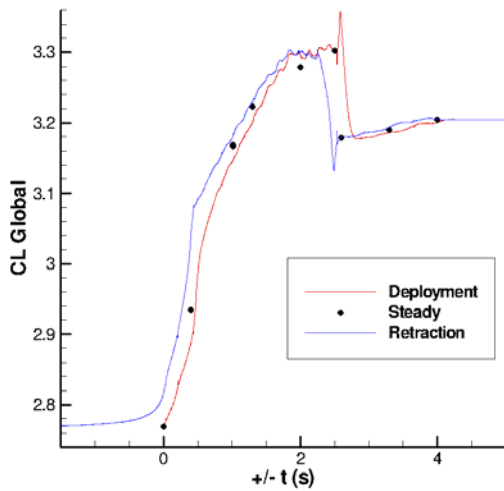


Figure 17: Cases 24 and 24 REV, Global CL.
(for retraction, time is reversed on the x axis)

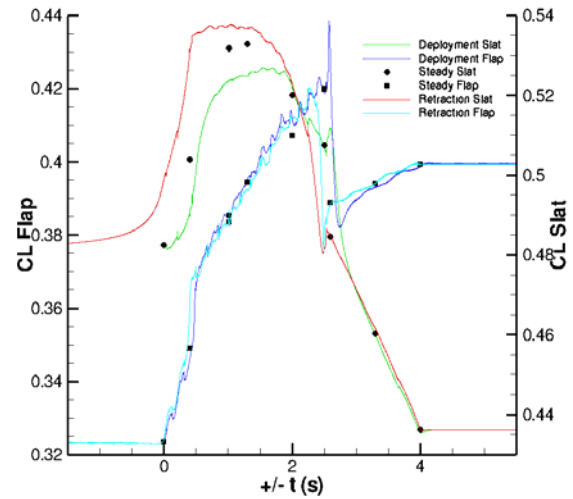


Figure 18: Cases 24 and 24 REV, Slat and Flap CL

The coefficients suddenly change near $t = 2.6$ s (deployment case). It is not caused by the end of the flap motion, as it happens before it. This huge decrease of the flap lift coefficient, also predicted for the steady solutions, results from a quick growth of the flow separation on the flap. Indeed, for many real transport aircraft, the flow detaches from the rear part of the flap at high deployment angles and moderate angles of attack. This is caused by a kink on the upper surface of the flap such that it fits to the main wing when fully retracted. This kink triggers flow separation when the flap is fully deployed, as shown on Figure 19. See part 5.5 for more details.

The separation starts later during the deployment case than it does for the steady solutions with the equivalent system settings. During the retraction, it disappears for even less deployed a setting. This suggests a flow delay of the order of the characteristic advection time of the airfoil. This cannot be described by the quasi-steady corrections previously presented, since the effect of the rotation tends to increase the load on the flap when it is deployed, which would lead to an earlier flow separation.

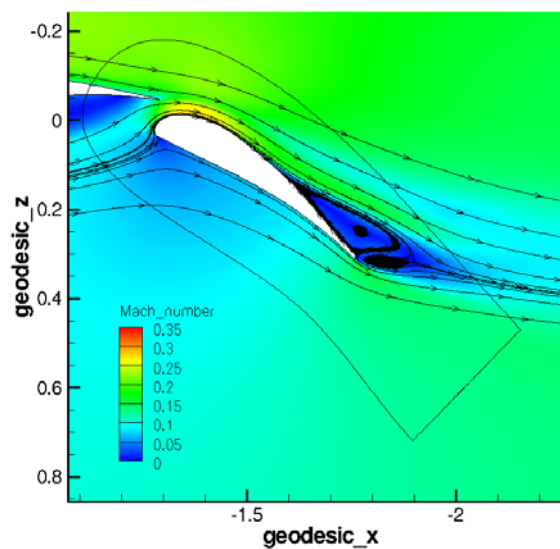


Figure 19: Flow separation on the flap, Pos. 4.
Mach number

Another striking feature is the gap between deployment and retraction from $t = 0$ s to $t = 2$ s (time of Case 24). Especially the slat has a much higher lift when it is retracted than when it is deployed. Figure 20 and Figure 21 respectively show the difference of pressure and Mach number between the retraction and the deployment. The difference of pressure on the flap seems to come from the quasi-steady effect of the rotation. The bubble in the slat cove seems to be smaller during the retraction than during the deployment.

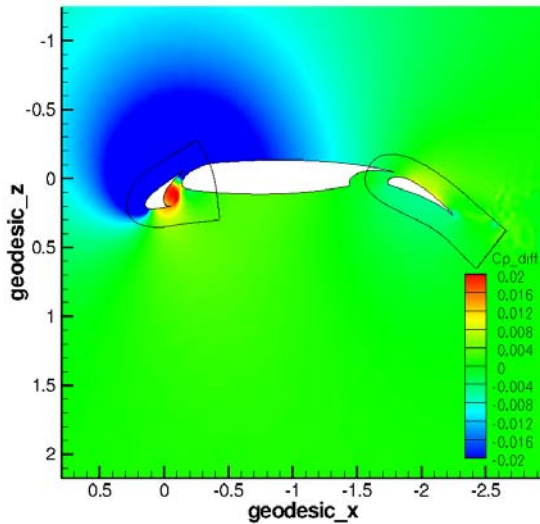


Figure 20: C_p difference, $t = 1.3$ s of Case 24.
Case 24 REV - Case 24.

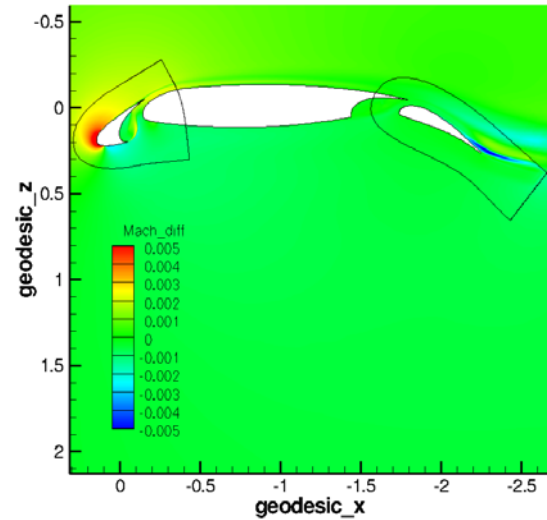


Figure 21: Mach difference, $t = 1.3$ s of Case 24.
Case 24 REV - Case 24.

Spectral analysis helps to separate the components of the time signal caused by the Chimera problem from components that may be more physical, like the oscillation on the time signal between $t = 3.0$ s and $t = 4.0$ s on Figure 17 and Figure 18. A discrete Fourier transform has been implemented, using a Hann window since the signal is not periodic. The signal is cut without introducing spurious frequencies thanks to the shape of this window.

Figure 22 shows the energy density of the Fourier transform of the global and flap lift coefficients, for Case 24 between $t = 3.0$ s and $t = 4.0$ s. There is a peak near 3Hz, which corresponds to the oscillation described on the time signal. It is not caused by the flap motion, which ended at $t = 2.6$ s. Multiplying by the characteristic advection time of the airfoil defined in 5.1 gives a Strouhal number of 0.12, a low value. Figure 23 shows that for the same case between $t = 1.5$ s and $t = 2.5$ s, this oscillation is already present, although it cannot be seen on the time signal. Figure 24 suggests that between $t = 1.0$ s and $t = 2.0$ s, the 3Hz peak has not yet appeared.

Another peak is located at approximately 192Hz, corresponding to a vortex shedding located at the trailing edge of the flap (see 5.6), with an associated Strouhal number of 2.1. The peak located near 7Hz is caused by the Chimera problem.

From the other simulated cases, it seems that the 3Hz oscillation is neither triggered by the motion of the flap nor by the motion of the slat, but if no element is moving at all, it disappears. The deployment angle of the flap has to be high enough for it to appear.

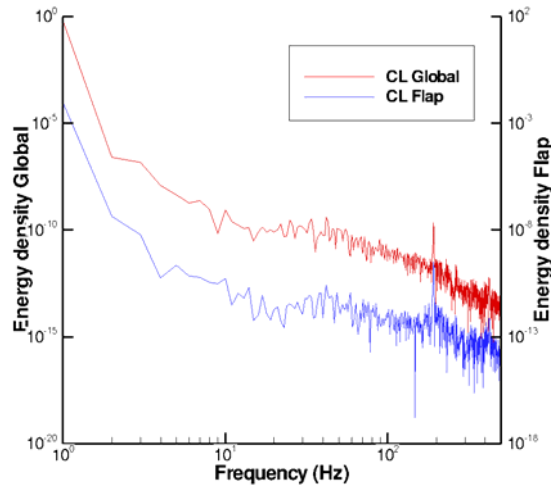


Figure 22: Case 24, Fourier window between $t = 3.0$ s and $t = 4.0$ s, Energy density.

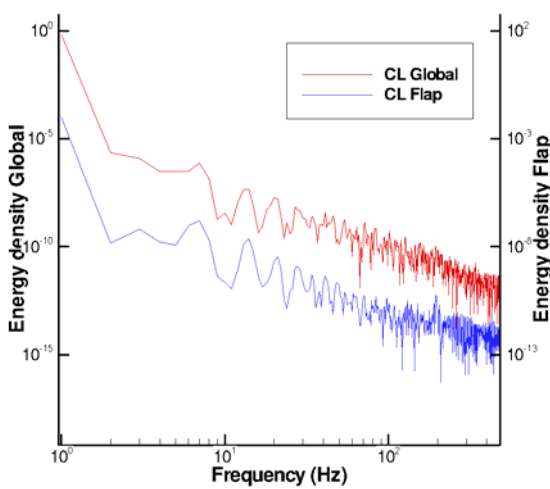


Figure 23: Case 24, Fourier window between $t = 1.5$ s and $t = 2.5$ s, Energy density.

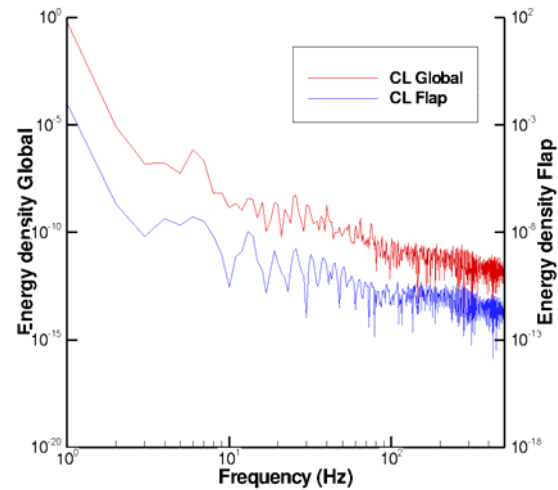


Figure 24: Case 24, Fourier window between $t = 1.0$ s and $t = 2.0$ s, Energy density.

5.4 Case 34

Only the slat is deployed, from $t = 5$ s to $t = 9$ s, whereas the flap is already in its maximum setting. Figure 25 and Figure 26 show the lift coefficients for each element. The lift of the slat decreases because its effective angle of attack is decreasing. The unsteady lift coefficient of the slat remains close to its steady value.

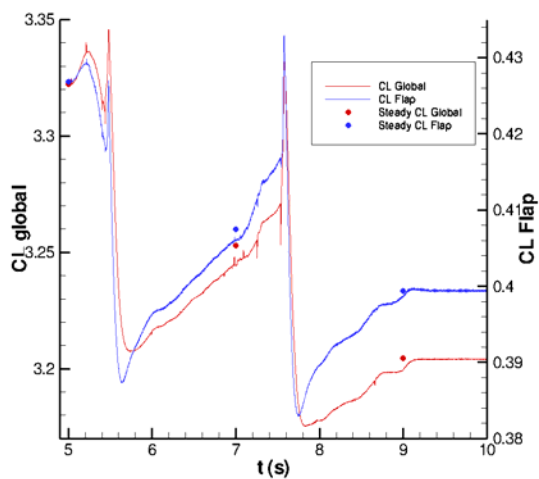


Figure 25: Case 34, slat motion from $t = 5$ s to 9s.
Global and flap CL

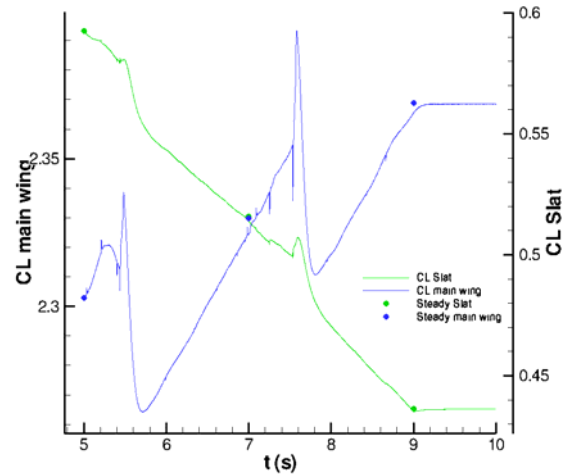


Figure 26: Case 34, slat motion from $t = 5$ s to 9s.
Slat and main wing CL.

The most striking feature of Case 34 is the abrupt decrease of the lift coefficient of the flap, as well as of the global and main wing lift coefficients, which happens twice, near $t = 5.6$ s and $t = 7.7$ s. This reveals the quick growth of the flow separation on the flap, which is similar to what happens in Case 24: see part 5.5.

5.5 Flow detachment on the flap in cases 24 and 34

The huge drop of lift, which happens twice in Case 34 and once in Case 24, is caused by the sudden development of the bubble on the upper surface of the flap. The deployment of the slat makes its effective angle of attack decrease. Because of the slat-effect (see reference [5]) the load on the flap increases. However, the flow detachment point stays behind the kink of the flap (see 5.3) during a long time, which limits the size of the bubble. When the detachment point moves in front of the kink of the flap, the bubble suddenly develops, and the lift dramatically decreases. Figure 27 ($t = 2.5$ s of Case 24) and Figure 28 ($t = 2.8$ s) show how different the flow topology is. In Case 34, the detachment point moves back aft of the kink before the second massive separation.

Another feature clearly visible on the time signals is that the lift coefficient of the flap first increases before it suddenly decreases. In the retraction case (Case 24 REV), on the contrary the lift coefficient first decreases before increasing dramatically.

However, the reason for this remains unclear. There may be a physical explanation, because the evolution of the pressure is strikingly similar in Cases 34 and 24, although the setting of the slat is very different.

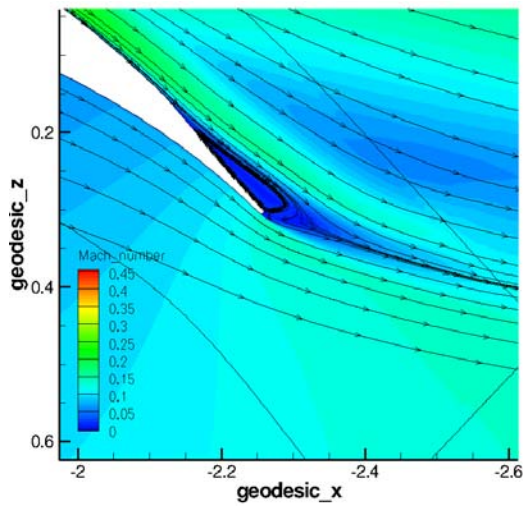


Figure 27: Case 24, $t = 2.500$ s. Mach number and streamlines.

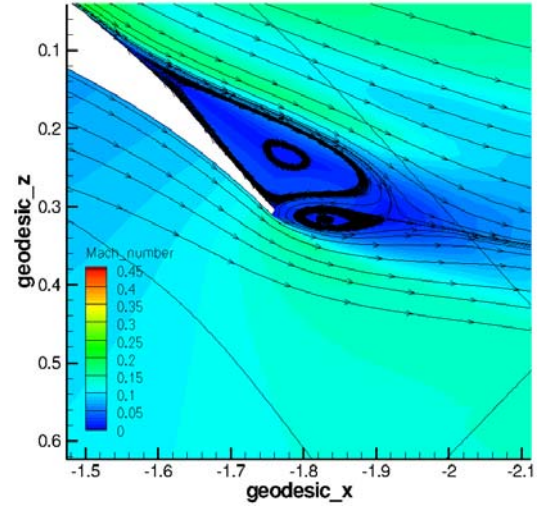


Figure 28: Case 24, $t = 2.800$ s. Mach number and streamlines.

5.6 Vortex shedding at the trailing edge of the flap

The frequency peak close to 190Hz (Strouhal number of 2.1, see part 5.3) is caused by a vortex shedding located at the trailing edge of the flap, as emphasized by Figure 29, which shows an approximation of the first partial time derivative of the vorticity. The vortex shedding happens when the deployment angle of the flap is high enough, but it does not depend on the extent of the bubble on the flap.

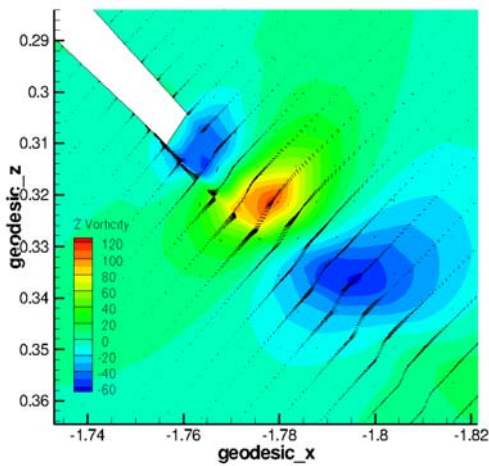


Figure 29: Difference (arrows) of the velocities at $t = 6.001 - 6.000$ s and its vorticity (s^{-1}) (colors), Case 24

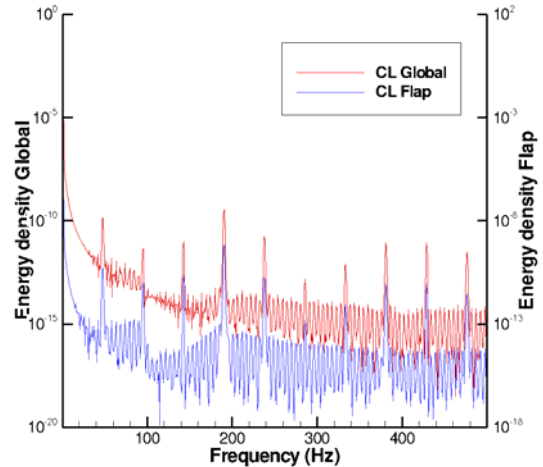


Figure 30: Case 24, Fourier window from $t = 6$ s to $t = 7$ s. Energy density, global and flap CL

After the end of the motion of the system, the energy spectrum evolves in a surprising way. For instance, Figure 30 shows the energy density for Case 24 with a window ranging from $t = 6$ s to $t = 7$ s (the motion of the slat ended at $t = 4$ s). Even though the frequency associated to the vortex shedding, at 190Hz, remains the strongest peak, it appears to be only a multiple of a fundamental frequency at 47Hz (multiplying by the advection characteristic time of the flap defined in 5.1 gives a Strouhal number of 0.52). All peaks are multiples of this first frequency. No physical explanation could be found for this phenomenon, and it seems to happen only in absence of motion of the flap and of the slat. Time step reduction tests suggest that the

frequencies of the peaks may have a physical origin, but their amplitude may be over-predicted because of too large a time step.

Besides, the energy spectrum is somewhat different when the system is set to another position. Even more surprisingly, when it is set to the same position but after a different sequence of flap and slat deployment, the spectrum is different as well. The common features between all cases is that the vortex shedding frequency is always the strongest peak, and is a multiple of a fundamental frequency, several other multiples of which are present.

6 CONCLUSIONS

In this work, numerical simulation of the unsteady flow around a high-lift airfoil during deployment of the high-lift devices has been presented. Several movements of the high-lift system between take-off and landing setting have been analyzed in deflection and retraction mode.

The study unveils significant time delays compared to steady state computations. Although, the time shift of the lift coefficient during the flap movement can be verified by quasi-steady analysis. For the slat flow the interaction seems too complicated to be correlated easily. It can turn out to be very important to take them into account for flight dynamics models or if a high-lift system were designed with higher a deployment speed. Moreover, some of the results cannot be simply described by means of a time delay applied to steady data. As for an observed low frequency oscillation, if its prediction is reliable, damping it could make the travel more comfortable.

The frequencies predicted for the quasi “steady” flows with a vortex shedding at the trailing edge of the flap, could be a good starting point for a computational aero-acoustics study, all the more as this does not last the short duration of the deployment of the system, but the whole time when the system is deployed. Wind-tunnel tests could be made, since in this case the flap and the slat do not move.

Some results still miss physical explanations to be sure they have no spurious origin: the 3 Hz oscillation, which could be an eigenmode of the flap, or the increase of lift preceding the growth of the separation bubble on the flap.

Only the lift was considered in this study, but it would be very interesting to analyze the other aerodynamic coefficients. This study was also limited by the impossibility to simulate a complete retraction of the high-lift system.

Unfortunately, the quality of the solutions is slightly corrupted by the artificial disturbances introduced by the Chimera method. Using finer meshes, which would have cells of more similar sizes in the overlapping regions passed through during deflection, could help reduce this issue. But even better solutions would be expected, if the value on a vertex in the middle of a large control volume were not interpolated from one cell to the other, but were instead the result of the integral over the control volume of the values taken on the finer mesh. This would be much more consistent with the finite volume formulation.

REFERENCES

- [1] P.K.C. Rudolph: High-Lift Systems on Commercial Subsonic Airliners. NASA CR 4746, Sept. 1996.
- [2] J. Wild: Experimental investigation of Mach- and Reynolds-number dependencies of the stall behavior of 2-element and 3-element high-lift wing sections. AIAA-Paper 2012-0108, *50th AIAA Aerospace Science Meeting*, Nashville, 9-12 Jan. 2012.

- [3] B. Holert: Eine Methode zum mehrkriteriellen Entwurf der Führungsmechanismen in Hochauftriebssystemen von Transportflugzeugen. PhD-thesis, TU Hamburg-Harburg, Schriftenreihe Flugzeug-Systemtechnik 2005:3, Shaker, Aachen, 2006.
- [4] <http://www.youtube.com/watch?v=EhMNpyOhSvU>: Video of the deployment and retraction sequences of the slats and flaps of the A320 from the point of view of a passenger, accessed 2011.
- [5] A.M.O. Smith: High Lift Aerodynamics (Wright Brothers Lecture). AIAA Paper No. 74-939, August 1974.
- [6] D. Schwamborn, T. Gerhold, R. Heinrich: The DLR Tau-Code: Recent Applications in Research and Industry. *ECCOMAS CFD 2006 conference*, Netherlands, 2006.
- [7] CentaurSoft, <http://www.centaursoft.com>.
- [8] O.Brodersen, M.Hepperle, A.Ronzheimer, C.-C.Rossow, B. Schöning: The Parametric Grid Generation System MegaCads. In: *Proc. 5th International Conference on Numerical Grid Generation in Computational Field Simulations*, NSF Engineering Research Center, Mississippi State University, 1996, pp. 353-362.
- [9] D.G. Crighton: The Kutta condition in unsteady flow. *Ann. Rev. Fluid Mech.*, 1985.17:411-45, 1985.